Draft version July 14, 2023
Typeset using LaTeX preprint style in AASTeX63

Stellar Cruise Control: Weakened Magnetic Braking Leads to Sustainted Rapid Rotation of Old Stars

Nicholas Saunders,[1,*] Jennifer L. van Saders,[1] Alexander J. Lyttle,[2,3]
Travis Metcalfe,[4,5] Tanda Li,[2,3] Guy R. Davies,[2,3] Oliver J. Hall,[6,7,8] Warrick Ball,[2,3]
Richard Townsend,[9,10] Orlagh Creevey,[11] and Curt Dodds[1]

[1]*Institute for Astronomy, University of Hawai'i at Mānoa, 2680 Woodlawn Drive, Honolulu, HI 96822, USA*
[2]*School of Physics and Astronomy, University of Birmingham, Birmingham, B15 2TT, UK*
[3]*Stellar Astrophysics Centre (SAC), Department of Physics and Astronomy, Aarhus University, Ny Munkegade 120, DK-8000 Aarhus C, Denmark*
[4]*Space Science Institute, 4765 Walnut St., Suite B, Boulder, CO 80301, USA*
[5]*White Dwarf Research Corporation, 3265 Foundry Pl., Unit 101, Boulder, CO 80301, USA*
[6]*European Space Agency (ESA), European Space Research and Technology Centre (ESTEC), Keplerlaan 1, 2201 AZ Noordwijk, The Netherlands*
[7]*School of Physics and Astronomy, University of Birmingham, Edgbaston, Birmingham, B15 2TT, UK*
[8]*Stellar Astrophysics Centre, Department of Physics and Astronomy, Aarhus University, Ny Munkegade 120, 8000 Aarhus C, Denmark*
[9]*Department of Astronomy, University of Wisconsin-Madison, 2535 Sterling Hall, 475 N. Charter Street, Madison, WI 53706, USA*
[10]*Kavli Institute for Theoretical Physics, University of California, Santa Barbara, CA 93106, USA*
[11]*Université Côte d'Azur, Observatoire de la Côte d'Azur, CNRS, Laboratoire Lagrange, Bd de l'Observatoire, CS 34229, 06304 Nice Cedex 4, France*

ABSTRACT

The ability to measure stellar ages and rotation rates with asteroseismology revealed an older population of stars with surprisingly rapid rotation rates. Sustained rapid rotation in old stars can potentially be explained by a departure from smooth rotational evolution caused by weakened magnetic braking during main sequence evolution. Despite a growing sample of precisely measured rotation periods, the strength of magnetic braking and the threshold for departure from standard spindown have remained persistent questions, particularly for stars more evolved than the sun. Rotation periods can be measured for stars older than the sun by leveraging asteroseismology, enabling models to be tested against a larger sample of old field stars. Because asteroseismic measurements of rotation do not depend on starspot modulation, they avoid potential biases introduced by the need for a stellar dynamo to drive starspot production. Using a neural network trained on a grid of stellar evolution models and a hierarchical model-fitting approach, we constrain the onset of weakened magnetic braking. We find that a sample of stars with asteroseismically-measured rotation periods and ages is consistent with models that depart from standard spindown prior to reaching the evolutionary stage of the sun. We test our approach using neural networks trained on model grids produced by separate stellar evolution codes and find mild disagreement, indicating that the choices of grid physics can influence the inferred properties of the braking law. We identify the normalized critical Rossby number $\mathrm{Ro_{crit}/Ro_\odot} = 0.91 \pm 0.04$ as the threshold for the departure from standard rotational evolution. This suggests that weakened magnetic braking poses challenges to gyrochronology for much of the main sequence lifetime of sun-like stars.

1. INTRODUCTION

Over their main sequence lifetimes, low-mass stars gradually lose angular momentum and slow their rotation due to magnetic braking (Weber & Davis 1967; Skumanich 1972). This angular momentum loss results from the interaction between a star's dynamo and stellar winds (Parker 1958; Kawaler 1988). The method of leveraging stellar rotation periods to estimate age, called *gyrochronology* (Barnes 2010; Epstein & Pinsonneault 2013), can provide constraints on age with ∼10% precision for sun-like stars (Meibom et al. 2015). Numerous studies have provided prescriptions for angular momentum loss (Kawaler 1988; Krishnamurthi et al. 1997; Sills et al. 2000; Barnes 2010; Denissenkov et al. 2010; Reiners & Mohanty 2012; Epstein & Pinsonneault 2013; Gallet & Bouvier 2013, 2015; Matt et al. 2015; van Saders et al. 2016), which can be empirically calibrated to observations. The relationship between rotation period and age has been well characterized for young and intermediate-age clusters (Barnes 2007, 2010; Mamajek & Hillenbrand 2008; Meibom et al. 2011, 2015; Angus et al. 2019; Dungee et al. 2022), where both properties can be constrained with adequate precision.

In essentially all of these calibrators, rotation rates are measured by observing spot modulation due to dark starspots rotating in and out of view. The *Kepler* Space Telescope (Borucki et al. 2010), and the subsequent *K2* mission (Howell et al. 2014), enabled predictions for magnetic braking to be tested on a wealth of open clusters and associations (see Cody et al. 2018) as well as a population of older field stars (McQuillan et al. 2014; Santos et al. 2021).

In addition to starspot modulation used to detect rotation, brightness modulations due to stellar oscillations are measurable in the high-precision, long-baseline *Kepler* time series photometry (Huber et al. 2011). Asteroseismology—the study of these oscillations—provides valuable information about the internal structure and evolution of stars. Specifically, the rotation rates (Nielsen et al. 2015; Davies et al. 2015; Hall et al. 2021) and ages (Metcalfe et al. 2014, 2016; Silva Aguirre et al. 2015; Creevey et al. 2017) of *Kepler* stars can be measured with asteroseismology.

When the rotation rates and ages of older, sun-like field stars were asteroseismically measured with *Kepler* data, they were found to maintain surprisingly rapid rotation late into their main sequence lifetimes (Angus et al. 2015). To explain this sustained rapid rotation, it was proposed that stars diverge from the "standard spindown" model and enter a phase of "weakened magnetic braking" (WMB; van Saders et al. 2016, 2019). As additional *Kepler* stars were analyzed with asteroseismology, their rotation periods were consistently overpredicted by the standard spindown model and evidence for WMB strengthened (Hall et al. 2021). Asteroseismology measures internal rotation rates in the stellar envelope, making it insensitive to surface differential rotation (Nielsen et al. 2015) and stellar inclination (Davies et al. 2015); additionally, asteroseismology can measure rotation rates for stars with weak surface magnetic activity and therefore undetectable spot modulation signals (Chaplin et al. 2011). These features allow asteroseismic rotation periods to avoid potential biases present in measurements from spot detection.

Careful analysis of pileups in the temperature-period distribution of sun-like stars also supported the WMB model. Studies of rotation rates in the *Kepler* field identified an upper envelope in stellar mass

* NSF Graduate Research Fellow, nksaun@hawaii.edu

versus rotation period that matched a gyrochrone at ∼4 Gyr (Matt et al. 2015). An upper edge to the distribution could be caused by either a magnetic transition or detection bias in spot modulation—however, forward modeling of the *Kepler* field supported the weakened braking scenario and predicted a pileup of rotation periods (van Saders et al. 2019). With refined measurements of stellar effective temperature, the predicted pileup in the temperature-period distribution was identified (David et al. 2022).

A study of sun-like stars with projected rotation periods measured from spectroscopic line broadening found them to be inconsistent with the Skumanich relation beyond ∼2 Gyr (dos Santos et al. 2016), supporting the weakened braking scenario. This sample was later revisited (Lorenzo-Oliveira et al. 2019), and the analysis suggested that the smooth rotational evolution scenario was favored, and if weakened braking takes place, it occurs at later times ($\gtrsim 5.3$ Gyr). All efforts to constrain a model for stellar spindown fundamentally depend on a reliable sample of calibrators, and the challenge of producing such a sample has hindered the development of a universally agreed-upon model.

The physical mechanism that would lead to WMB remains uncertain, though some have proposed that a transition in the complexity of the magnetic field could reduce magnetic braking efficiency (Réville et al. 2015; Garraffo et al. 2016; van Saders et al. 2016; Metcalfe et al. 2016, 2019). Because the transition may to be rooted in the strength and morphology of the magnetic field, it is challenging to test with surface rotation rates, which require active stellar dynamos to drive starspot production (Matt et al. 2015; Reinhold et al. 2020).

To effectively use gyrochronology to estimate stellar ages, it is essential to understand when the transition to weakened braking occurs. Previous studies have provided estimates for the onset of WMB (van Saders et al. 2016, 2019; David et al. 2022), but a full hierarchical model for the braking law has not been previously performed. As the departure from standard spindown depends on the dimensionless Rossby number and is predicted to be shared between all stars (van Saders & Pinsonneault 2013; van Saders et al. 2016), the problem is inherently hierarchical. Here, we provide new constraints on the evolutionary phase at which stars undergo weakened braking. We build on previous efforts (e.g. Hall et al. 2021) by modeling the rotational evolution of each star individually.

We apply a Hierarchical Bayesian Model (HBM) to constrain the population-level parameters for a WMB model. The use of an HBM has been shown to increase the precision of inferred stellar properties for high-dimensional models (Lyttle et al. 2021). Here, we model the weakened braking parameters as global properties shared by all stars, while simultaneously fitting individual stellar properties. We test the results of our fit using multiple model grids, and compare the performance of a WMB model to standard spindown. By comparing results between multiple model grids, we provide the first constraints on biases introduced by the choices of grid physics when modeling stellar rotational evolution. We find that weakened braking likely occurs before stars reach the evolutionary phase of the sun.

2. DATA

We fit our rotational model to open clusters, the sun, and *Kepler* field stars with asteroseismic measurements to ensure that we capture the early rotational evolution prior to the onset of weakened braking in addition to the behavior on the latter half of the main sequence. We limit our sample to stars within 0.2 $M_\odot$ of the sun to focus on the impacts of weakened braking. Stars hotter than $\sim$1.2 $M_\odot$ have radiative rather than convective envelopes on the main sequence, and do not undergo significant magnetic braking, and stars cooler than $\sim$0.8 $M_\odot$ are sensitive to early effects such as

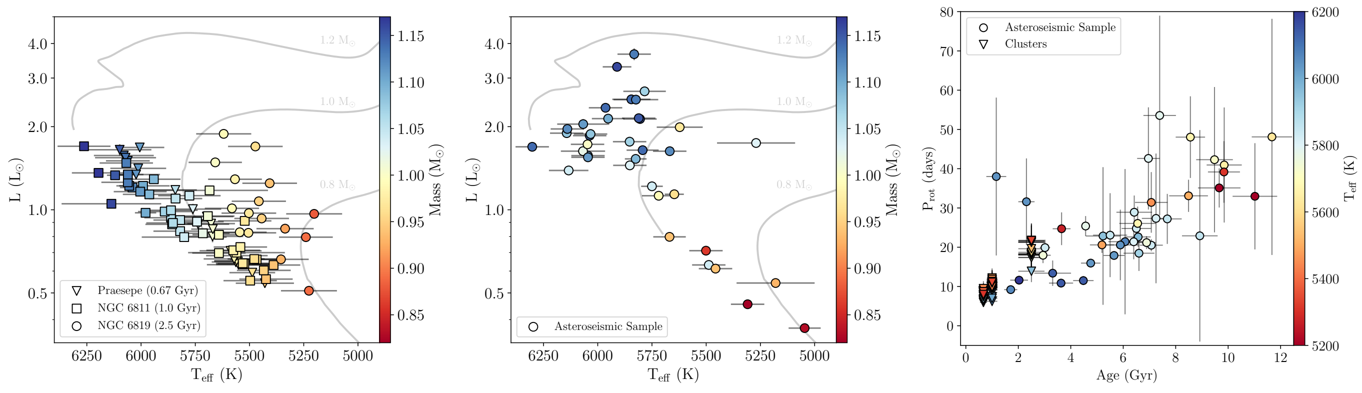

(a) (b) (c)

Figure 1. **(a)** Hertzsprung-Russell diagram showing our sample of calibrators in open clusters. Model tracks generated by our emulator are shown as gray lines. **(b)** Hertzsprung-Russell diagram of our asteroseismic sample from Hall21. We derived the stellar properties shown here with asteroseismic modeling. **(c)** Observed rotation period plotted as a function of stellar age. We color points by their effective temperature. Asteroseismic stars are shown as circles and open cluster members are marked by triangles.

the lifetime of a disk and the timescale for disk locking. We describe our calibrator sources in the following section.

2.1. *Open Clusters*

We included stars from the following open clusters: 23 stars in Praesepe (0.67 ± 0.134 Gyr; [Fe/H] $= 0.15 \pm 0.1$ dex; Rebull et al. 2017), 45 stars in NGC 6811 (1.0 ± 0.2 Gyr; [Fe/H] $= 0.0 \pm 0.04$ dex; Meibom et al. 2011; Curtis et al. 2019), and 17 stars in NGC 6819 (2.5 ± 0.5 Gyr; [Fe/H] $= 0.10 \pm 0.03$ dex; Meibom et al. 2015). We select stars within the $T_{\rm eff}$ range of our asteroseismic sample (5200 K $\leq T_{\rm eff} \leq$ 6200 K), using values for $T_{\rm eff}$ reported in Curtis et al. (2020). Ages and metallicities were taken from the corresponding cluster reference, and were used to define priors in our fitting.

2.2. *Asteroseismic Sample*

We also included a sample of *Kepler* field stars with asteroseismically-measured rotation rates and ages from Hall et al. (2021, hereafter Hall21). Rotation rates for main sequence stars can be difficult by observing periodic starspot modulation, particularly for older and less active stars, due to long rotation periods and diminished stellar activity. However, the rotational splitting of asteroseismic oscillation frequencies can be observed for stars in the end stages of the main sequence, and provides invaluable benchmarks for WMB.

Hall et al. (2021) used asteroseismic mode splitting to measure rotation periods for 91 *Kepler* dwarfs. We augmented the Hall21 sample with two additional stars with asteroseismic rotation measurements in the binary system HD 176465 (KIC 10124866; White et al. 2017). The A and B components of this system are sometimes referred to by their nicknames *Luke* and *Leia*, respectively. The rotation periods reported in White et al. (2017) were derived by fitting asteroseismic mode splitting, following the same approach as Hall21.

We made the following mass cut to ensure our sample would fall within the bounds of our model grid:

$$M + 1.5\sigma_M < 1.2 M_\odot$$

for a star's mass M and mass uncertainty σ_M.

We performed asteroseismic modeling for Luke & Leia and a subset of the Hall21 sample using version 2.0 of the Asteroseismic Modeling Portal[1] (AMP; Metcalfe et al. 2009; Woitaszek et al. 2009). This optimization method couples a parallel genetic algorithm (Metcalfe & Charbonneau 2003) with MESA stellar evolution models (Paxton et al. 2019) and the GYRE pulsation code (Townsend & Teitler 2013) to determine the stellar properties that most closely reproduce the observed oscillation frequencies and spectroscopic constraints for each star. The choices of input physics are nearly all the default choices in MESA release r12778, and the models include gravitational settling of helium and heavy elements (Thoul et al. 1994) as well as the two-term correction for surface effects proposed by Ball & Gizon (2014). The resulting asteroseismic sample is shown in panel (b) of Figure 1, while the stellar properties and rotation periods can be found in Table 1, which includes maximum-likelihood estimates of the age, mass, composition, and mixing-length from our AMP modeling.

3. METHODS

We produced model grids using two stellar evolution codes—Modules for Experiments in Stellar Astrophysics (MESA; Paxton et al. 2010, 2013, 2015, 2018, 2019) and Yale Rotating Stellar Evolution Code (YREC; Pinsonneault et al. 1989; Demarque et al. 2008). The ranges of stellar properties covered by our grid are detailed in Table 2, and we describe the model physics used to generate each grid in the following sections.

3.1. *MESA Model Grid*

We construct our MESA grid with identical input physics to the models used for asteroseismic inference (described in §2.2) in order to avoid biases introduced by the modeling (see Tayar et al. 2020). Our models used initial elemental abundances from Grevesse & Sauval (1998) and an atmospheric temperature structure following an Eddington $T(\tau)$ relation with fixed opacity. We smoothly ramp diffusion from fully modeled at M $\leq$ 1.1 M$_\odot$ to no diffusion at M $\geq$ 1.2 M$_\odot$. We do not include core or envelope overshoot. We varied the mass M, metallicity [Fe/H], initial Helium abundance $Y_{\rm init}$, and mixing length parameter $\alpha_{\rm MLT}$. We calculated rotational evolution histories for each combination of stellar properties and appended them to our grid.

By default, MESA models do not include the necessary stellar parameters to perform rotational evolution, and it was necessary to adapt the outputs included in the grid. The additional parameters we include for each star were the total moment of inertia $I_{\rm tot}$, the moment of inertia of the convective envelope $I_{\rm env}$, the photospheric pressure $P_{\rm phot}$, and the convective overturn timescale $\tau_{\rm cz}$. We define $\tau_{\rm cz}$ as

$$\tau_{\rm cz} = \frac{H_P}{v_{\rm conv}}$$

where H_P is the pressure scale height at the convective zone boundary and $v_{\rm conv}$ is the convective velocity one pressure scale height above the base of the convective zone. MESA does not store these values as the stellar model evolves, requiring us to modify the auxiliary run_star_extras.f file and augment the default MESA history files.

Stellar interiors in MESA models are divided into shells and the parameters are only calculated at each shell boundary. We identified the precise location of the base of the convective zone as a

[1] github.com/travismetcalfe/amp2

KIC	Age (Gyr)	$P_{\rm rot}$ (days)	M ($M_\odot$)	$T_{\rm eff}$ (K)	[Fe/H] (dex)	$Y_{\rm init}$	$\alpha_{\rm MLT}$
10644253	1.16 ± 0.38	38.01 ± 20.11	1.11 ± 0.05	6045 ± 77	0.06 ± 0.10	0.29 ± 0.03	1.66 ± 0.10
8379927	1.71 ± 0.25	9.20 ± 0.24	1.11 ± 0.04	6067 ± 120	-0.10 ± 0.15	0.26 ± 0.02	1.84 ± 0.15
9139151	2.03 ± 0.34	11.61 ± 0.94	1.14 ± 0.02	6302 ± 77	0.10 ± 0.10	0.26 ± 0.02	1.70 ± 0.09
3427720	2.31 ± 0.31	31.59 ± 11.03	1.11 ± 0.04	6045 ± 77	-0.06 ± 0.10	0.27 ± 0.02	1.72 ± 0.08
10124866B	2.94 ± 0.29	17.95 ± 2.00	0.97 ± 0.03	5745 ± 94	-0.30 ± 0.06	0.24 ± 0.01	1.84 ± 0.13
10124866A	3.02 ± 0.20	19.90 ± 2.00	0.95 ± 0.02	5831 ± 93	-0.30 ± 0.06	0.25 ± 0.01	1.62 ± 0.10
4141376	3.31 ± 0.70	13.39 ± 3.24	1.04 ± 0.04	6134 ± 91	-0.24 ± 0.10	0.25 ± 0.02	1.82 ± 0.12
8394589	3.63 ± 0.46	10.86 ± 0.58	1.08 ± 0.02	6143 ± 77	-0.29 ± 0.10	0.26 ± 0.01	1.78 ± 0.10
9025370	3.65 ± 0.34	24.71 ± 4.17	1.03 ± 0.03	5270 ± 180	-0.12 ± 0.18	0.25 ± 0.01	2.58 ± 0.18
10963065	4.48 ± 0.39	11.51 ± 1.14	1.12 ± 0.03	6140 ± 77	-0.19 ± 0.10	0.24 ± 0.02	1.74 ± 0.08
6106415	4.76 ± 0.37	15.95 ± 0.74	1.14 ± 0.02	6037 ± 77	-0.04 ± 0.10	0.23 ± 0.01	1.72 ± 0.06
8006161	5.19 ± 0.46	20.60 ± 2.04	1.04 ± 0.02	5488 ± 77	0.34 ± 0.10	0.25 ± 0.01	1.98 ± 0.09
5094751	5.23 ± 0.66	22.86 ± 17.53	1.10 ± 0.03	5952 ± 75	-0.08 ± 0.10	0.28 ± 0.02	1.66 ± 0.11
4914423	5.50 ± 0.65	23.07 ± 10.69	1.14 ± 0.03	5845 ± 88	0.07 ± 0.11	0.27 ± 0.02	1.68 ± 0.16
6116048	5.65 ± 0.40	17.90 ± 1.02	1.08 ± 0.02	6033 ± 77	-0.23 ± 0.10	0.25 ± 0.01	1.76 ± 0.07
9410862	5.89 ± 0.67	20.58 ± 8.99	1.00 ± 0.03	6047 ± 77	-0.31 ± 0.10	0.26 ± 0.02	1.80 ± 0.12
7106245	6.07 ± 0.64	21.41 ± 18.50	1.02 ± 0.02	6068 ± 102	-0.99 ± 0.19	0.22 ± 0.02	1.76 ± 0.13
4914923	6.40 ± 0.51	21.39 ± 4.47	1.15 ± 0.03	5805 ± 77	0.08 ± 0.10	0.24 ± 0.02	1.68 ± 0.08
6933899	6.42 ± 0.68	28.91 ± 4.27	1.13 ± 0.03	5832 ± 77	-0.01 ± 0.10	0.27 ± 0.02	1.68 ± 0.11
6521045	6.50 ± 0.56	24.78 ± 1.94	1.13 ± 0.02	5824 ± 103	0.02 ± 0.10	0.26 ± 0.02	1.68 ± 0.09
3544595	6.55 ± 0.70	26.06 ± 4.29	0.94 ± 0.03	5669 ± 75	-0.18 ± 0.10	0.25 ± 0.02	1.88 ± 0.11
10516096	6.57 ± 0.48	22.62 ± 2.52	1.14 ± 0.02	5964 ± 77	-0.11 ± 0.10	0.24 ± 0.01	1.72 ± 0.07
11401755	6.60 ± 0.59	18.48 ± 4.52	1.16 ± 0.02	5911 ± 66	-0.20 ± 0.06	0.22 ± 0.02	1.72 ± 0.13
12069449	6.89 ± 0.35	21.18 ± 1.64	1.04 ± 0.01	5750 ± 50	0.05 ± 0.02	0.26 ± 0.01	1.84 ± 0.05
11295426	6.96 ± 0.43	42.61 ± 13.02	1.14 ± 0.02	5793 ± 74	0.12 ± 0.07	0.22 ± 0.01	1.76 ± 0.05
12069424	7.07 ± 0.44	20.52 ± 1.54	1.09 ± 0.02	5825 ± 50	0.10 ± 0.03	0.25 ± 0.01	1.76 ± 0.05
9955598	7.07 ± 0.62	31.41 ± 7.72	0.94 ± 0.03	5457 ± 77	0.05 ± 0.10	0.25 ± 0.02	1.92 ± 0.12
7680114	7.25 ± 0.54	27.34 ± 16.52	1.15 ± 0.02	5811 ± 77	0.05 ± 0.10	0.24 ± 0.02	1.74 ± 0.07
10514430	7.39 ± 0.62	53.56 ± 25.42	1.07 ± 0.05	5784 ± 98	-0.11 ± 0.11	0.27 ± 0.03	1.78 ± 0.09
9098294	7.68 ± 0.55	27.21 ± 6.37	1.03 ± 0.02	5852 ± 77	-0.18 ± 0.10	0.25 ± 0.01	1.86 ± 0.08
7871531	8.49 ± 0.74	33.09 ± 4.10	0.86 ± 0.02	5501 ± 77	-0.26 ± 0.10	0.28 ± 0.01	1.94 ± 0.11
3656476	8.56 ± 0.56	48.04 ± 10.40	1.12 ± 0.02	5668 ± 77	0.25 ± 0.10	0.26 ± 0.01	1.80 ± 0.04
5950854	8.92 ± 0.68	22.91 ± 26.94	1.07 ± 0.04	5853 ± 77	-0.23 ± 0.10	0.22 ± 0.01	1.92 ± 0.12
8424992	9.48 ± 0.70	42.30 ± 18.51	0.99 ± 0.03	5719 ± 77	-0.12 ± 0.10	0.23 ± 0.02	1.90 ± 0.09
11772920	9.66 ± 0.81	35.11 ± 4.99	0.93 ± 0.05	5180 ± 180	-0.09 ± 0.18	0.23 ± 0.01	2.16 ± 0.28
7970740	9.84 ± 0.61	39.17 ± 7.85	0.81 ± 0.02	5309 ± 77	-0.54 ± 0.10	0.27 ± 0.02	2.14 ± 0.11
11904151	9.85 ± 0.67	40.94 ± 14.66	0.96 ± 0.02	5647 ± 44	-0.15 ± 0.10	0.25 ± 0.02	1.84 ± 0.07
6278762	11.02 ± 0.85	32.97 ± 13.53	0.83 ± 0.02	5046 ± 74	-0.37 ± 0.09	0.22 ± 0.02	2.42 ± 0.19
4143755	11.67 ± 0.77	48.10 ± 30.07	0.97 ± 0.04	5622 ± 106	-0.40 ± 0.11	0.23 ± 0.02	1.78 ± 0.13

Table 1. The sample of 39 asteroseismic *Kepler* field stars used in our fit. The rotation periods for 10124866A & B are from White et al. (2017), all other rotation periods taken from Hall et al. (2021). Other stellar properties were derived for this work using asteroseismic mode fitting.

Parameter		MESA Bounds	YREC Bounds
Mass	M ($M_\odot$)	[0.8, 1.2]	[0.8, 1.2]
Mixing Length Parameter	$\alpha_{\rm MLT}$	[1.4, 2.0]	[1.4, 2.0]
Metallicity	[Fe/H] (dex)	[-0.3, 0.3]	[-0.3, 0.3]
Initial Helium Abundance	$Y_{\rm init}$	[0.22, 0.28]	*not varied*
Braking Law Strength	f_K	[4.0, 11.0]	[4.0, 11.0]
Critical Rossby Number	$\rm Ro_{crit}$	[1.0, 4.5]	[1.0, 4.5]

Table 2. Parameter boundaries of the MESA and YREC grids.

function of the star's mass fraction using the Schwarzschild criterion, and then interpolated between the values calculated at each shell boundary to more precisely identify the values of our desired parameters at each time step. We remove the pre-main sequence from our tracks, defined as the threshold at which the luminosity from nuclear burning exceeds 99% of the total stellar luminosity. We allow the tracks to begin evolving up the subgiant branch, as our sample includes stars at or approaching this evolutionary stage, but remove tracks that exceed a rotation period of 150 days.

3.2. *YREC Model Grid*

We construct our YREC grid following the settings laid out in van Saders & Pinsonneault (2013) and Metcalfe et al. (2020). We use the mixing length theory of convection (Vitense 1953; Cox & Giuli 1968) with the 2006 OPAL equation of state (Rogers et al. 1996; Rogers & Nayfonov 2002). Abundances were taken from Grevesse & Sauval (1998) and opacities from the Opacity Project (Mendoza et al. 2007). We define atmosphere and boundary conditions from Kurucz (1997). Nuclear reaction rates were drawn from Adelberger et al. (2011). We varied the same parameters as we did for the MESA grid, with the exception of $Y_{\rm init}$.

As with the MESA grid, we trace additional parameters to evaluate the angular momentum loss law. For each model at each timestep, we calculate the moment of inertia of both the star and its convective envelope, the photospheric pressure, and the convective overturn timescale. We follow the same treatment described in §3.1 to remove the pre-main sequence and late-stage evolution from our YREC tracks.

3.3. *Magnetic Braking Model*

Prescriptions for magnetic braking often rely on the dimensionless Rossby Number (Ro), defined as the ratio between the rotation period, P, and convective overturn timescale within the stellar envelope, $\tau_{\rm CZ}$. We use the Rossby number in our rotation model due to its utility as a tracer for both the mass and composition dependence of spindown and magnetic field strength. We invoke a Rossby threshold, $\rm Ro_{crit}$, beyond which point stars depart from a simple power law spindown and conserve angular momentum (van Saders et al. 2016). We adopt the Matt et al. (2012) modification to the Kawaler (1988) braking law. We assume, as in van Saders & Pinsonneault (2013), that the magnetic field strength B scales as $B \propto \rm P_{phot}^{1/2} \propto Ro^{-1}$, where $\rm P_{phot}$ is the photospheric pressure, and that mass loss $\dot{M}$ scales as $\dot{M} \propto L_X \propto L_{\rm bol}{\rm Ro}^{-2}$, where L_X is the x-ray luminosity and $L_{\rm bol}$ is the bolometric luminosity.

Our full model for rotational evolution is described by

$$\frac{\mathrm{d}J}{\mathrm{d}t} = \begin{cases} f_K K_M \omega \left(\frac{\omega_{\mathrm{sat}}}{\omega_\odot}\right)^2, & \omega_{\mathrm{sat}} \leq \omega \frac{\tau_{\mathrm{cz}}}{\tau_{\mathrm{cz},\odot}}, \mathrm{Ro} \leq \mathrm{Ro}_{\mathrm{crit}} \\ f_K K_M \omega \left(\frac{\omega \tau_{\mathrm{cz}}}{\omega_\odot \tau_{\mathrm{cz},\odot}}\right)^2, & \omega_{\mathrm{sat}} > \omega \frac{\tau_{\mathrm{cz}}}{\tau_{\mathrm{cz},\odot}}, \mathrm{Ro} \leq \mathrm{Ro}_{\mathrm{crit}} \\ 0, & \mathrm{Ro} > \mathrm{Ro}_{\mathrm{crit}} \end{cases}$$

where Ro is defined as

$$\mathrm{Ro} = \frac{P}{\tau_{\mathrm{cz}}},$$

f_K is the scaling factor for the strength of angular momentum loss during classical spindown, ω_{sat} is the threshold at which angular momentum loss saturates for young stars, and with

$$\frac{K_M}{K_{M,\odot}} = c(\omega) \left(\frac{R}{R_\odot}\right)^{3.1} \left(\frac{M}{M_\odot}\right)^{-0.22} \left(\frac{L}{L_\odot}\right)^{0.56} \left(\frac{P_{\mathrm{phot}}}{P_{\mathrm{phot},\odot}}\right)^{0.44}.$$

We focus only on f_K and $\mathrm{Ro}_{\mathrm{crit}}$ as they will be the most dominant parameters of a WMB law for the stars in our sample, which are old enough to have converged onto tight rotation sequences (Epstein & Pinsonneault 2013; Gallet & Bouvier 2015). We assume a disk locking period of 8.13 days and disk lifetime of 0.28 Myr, setting the initial rotation rates of our models. We fix ω_{sat} to 3.863 $\times 10^{-5}$ rad/s. Each of these parameters will be important at early (< 100 Myr) times, but will have negligible effects by the time stars reach the ages in our sample. We assume solid body rotation in our models, since the epoch of radial differential rotation in this mass range is again limited to young stars (Denissenkov et al. 2010; Gallet & Bouvier 2015; Spada & Lanzafame 2020).

3.4. *Model Grid Emulator*

With fully rotationally evolved model grids, we construct an emulator for rapid stellar evolution modeling. The general approach to this type of optimization problem is simple interpolation between tracks in a high-dimensional model grid (e.g. Berger et al. 2020). However, due to the size of the grid, number of parameters (4-5 per star and cluster, with 2 additional global braking law parameters), and large sample of potential targets, this approach becomes computationally expensive, particularly in the application of Bayesian inference through sampling the model. We therefore opt to train an artificial neural network (ANN) to map the stellar parameters of the grid to observable parameters of stars in our sample.

We define our MESA ANN with seven input parameters and four output parameters. Our inputs represent fundamental stellar properties: age, mass, metallicity, initial Helium abundance, mixing length parameter, braking law strength, and critical Rossby number. The ANN outputs are observable quantities: effective temperature, radius, surface metallicity, and rotation period. The YREC ANN has the above input parameters with Y_{init} excluded, and identical output parameters. The remainder of this section describes the training and characterization of the MESA ANN. The process for training the YREC ANN is identical, and we compare the results when using different grids in §5.4.

Our model structure results in a neural network that acts as a stellar evolution emulator. Given some set of input stellar properties, the model will output the corresponding observable quantities. Because the emulation is rapid, the model can also be used in the inverse direction—given some set of observed properties, we can sample prior distributions for the underlying stellar properties and retrieve posterior distributions, providing estimates for these values with uncertainties.

We construct an ANN with 6 hidden layers comprised of 128 neurons each (following the tuning process of Lyttle et al. 2021). Each hidden layer used an Exponential Linear Unit (ELU) activation function. Using TensorFlow (Abadi et al. 2016), we trained the model on an NVidia Tesla V100 graphics processing unit (GPU) for 10,000 epochs using an *Adam* optimizer (Kingma & Ba 2017) with a learning rate of 10^{-5}. We trained the ANN in ∼8,000 batches of ∼16,000 points.

In order to ensure that the mapping performed by the neural network does not introduce significant uncertainty to the inferred parameters, we divide the grid data into a training set and a validation set. The training set is composed of 80% of the models in the grid, drawn at random, and is used to generate the connections between the input model parameters and observed stellar properties. The remaining 20% of the grid is then used to predict the observed parameters based on the provided input parameters, allowing us to characterize the neural network's ability to successfully predict well understood values. When compared to the measurement uncertainties associated with these parameters, the error introduced by the ANN is negligible, with typical fractional uncertainties of $\sim 10^{-3}$ in the recovery of our test set (see Figure 2). We also find negligible systematic offset for parameters in our test set, indicating that the ANN is not introducing any bias.

3.5. *Statistical Modelling*

In order to efficiently optimize the braking law model parameters, we construct a hierarchical Bayesian model (HBM). The application of a similar HBM for constraining the distribution of $Y_{\rm init}$ and $\alpha_{\rm MLT}$ has been demonstrated by Lyttle et al. (2021). We begin the construction of our model with Bayes' theorem—the posterior probability of our model parameters $\boldsymbol{\theta}_i$ given some set of observed data $\mathbf{d}_i$ is

$$p(\boldsymbol{\theta}_i|\mathbf{d}_i) \propto p(\boldsymbol{\theta}_i)p(\mathbf{d}_i|\boldsymbol{\theta}_i)$$

where $p(\boldsymbol{\theta}_i)$ is the prior on the model parameter i and $p(\mathbf{d}_i|\boldsymbol{\theta}_i)$ is the likelihood of the data given the model. We use our trained ANN to sample the prior distribution $p(\boldsymbol{\theta}_i)$ for each parameter and evaluate an instance of the model $\boldsymbol{\mu}_i = \boldsymbol{\lambda}_i(\boldsymbol{\theta}_i)$, where $\boldsymbol{\lambda}_i$ represents the ANN model. From this, we can represent the likelihood of each observation $\mathbf{d}_i$ with uncertainty $\boldsymbol{\sigma}_i$ given the model evaluation $\boldsymbol{\mu}_i$ as the normal distribution

$$p(\mathbf{d}_i|\boldsymbol{\theta}_i) = \prod_{n=1}^{N} \frac{1}{\sigma_{n,i}\sqrt{2\pi}} \exp\left[-\frac{(d_{n,i}-\mu_{n,i})^2}{2\sigma_{n,i}^2}\right]$$

given N observed variables.

The hierarchical structure of our model allows us to prescribe various levels of pooling to different parameters. The WMB model parameters f_K and $\mathrm{Ro}_{\rm crit}$, for example, are assumed to be the same for all stars in our sample. For the ANNs trained on both the the MESA and YREC grids, we define the prior for $\mathrm{Ro}_{\rm crit}$ as

$$\mathrm{Ro}_{\rm crit} \sim \mathcal{U}(1.0, 4.5)$$

and the prior for f_K as

$$f_K \sim \mathcal{U}(4.0, 11.0)$$

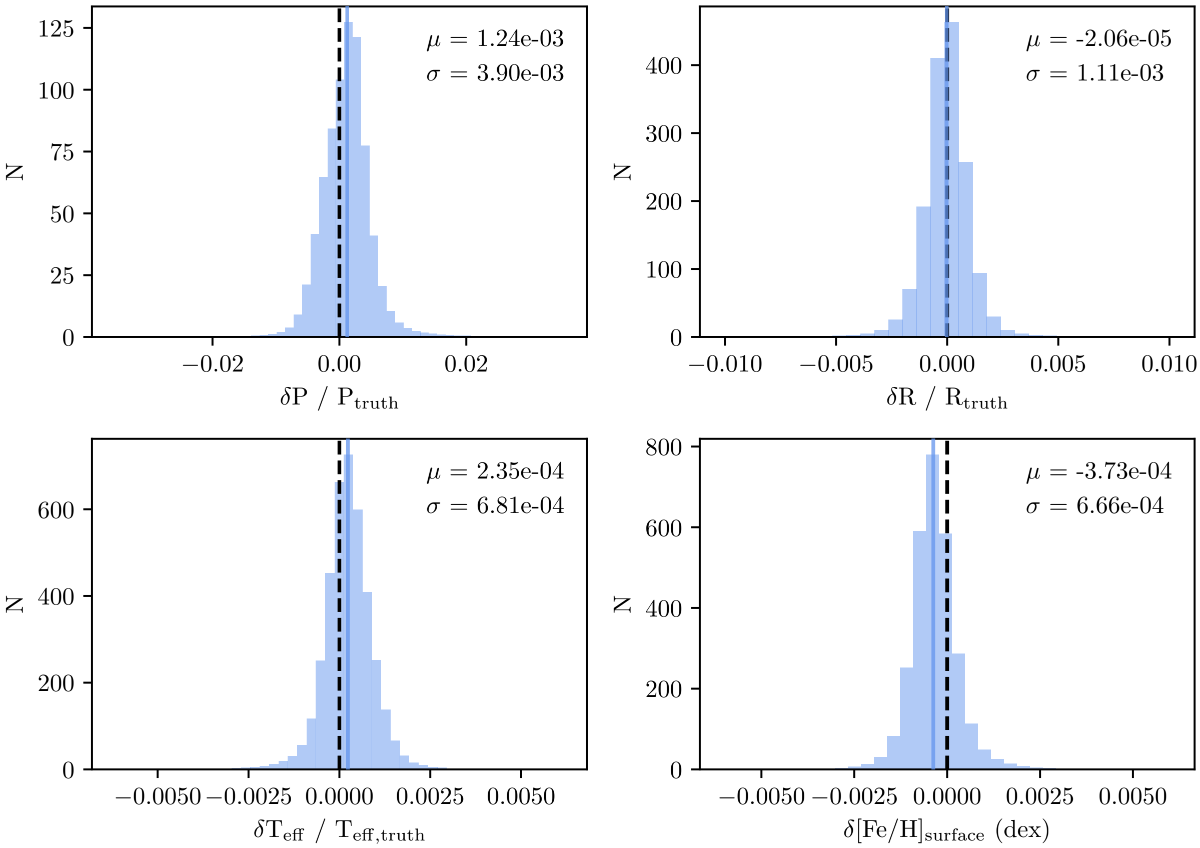

Figure 2. Uncertainty introduced by the MESA ANN emulator. The histograms for P, R, and $T_{\rm eff}$ show the (predicted−truth)/truth value for our training set, and the bottom right panel shows predicted−truth for the surface metallicity to account for points where $[{\rm Fe/H}]_{\rm surface,truth} \approx 0$. The median μ and standard deviation σ of these distributions are shown in the top right corner for each parameter, and μ is marked by the solid vertical line. The error incurred by the ANN is negligible compared to the uncertainty on the observed values.

where $\theta \sim X$ represents a parameter θ being randomly drawn from a distribution X, and $\mathcal{U}(a, b)$ is a uniform distribution bounded between a and b. The values of $\rm Ro_{crit}$ and f_K drawn from these uniform distributions are used to calculate the full set of model evaluations $\boldsymbol{\mu}_i$ for that step.

Other parameters are assumed to be unique to each star. For the YREC ANN, we constrain the mass, metallicity, mixing length parameter, effective temperature, and rotation period. We constrain the same parameters for the MESA ANN with the addition of the initial Helium abundance. The prior distributions for these parameters are defined as truncated normal distributions, given by

$$p(\boldsymbol{\theta}) \sim \mathcal{N}_{[a,b]}(\mu, \sigma)$$

where $\mathcal{N}$ is the normal distribution, a and b are the lower and upper bounds, respectively, μ is the median and σ is the standard deviation. Here, μ and σ are taken from the observational constraints on the parameters and their uncertainties. For stars in clusters, we define a prior centered on the value reported in the corresponding reference (see §2.1) with a width set to the measurement uncertainty for age, metallicity, rotation period, and effective temperature. For the masses of cluster stars, we use a homology scaling relationship with $T_{\rm eff}$ and set a broad prior (0.25 $M_\odot$), and for the mixing length parameter and initial Helium abundance, we use uniform priors. For asteroseismic stars in our sample, all of the above properties are constrained by the asteroseismic fitting, and we use the reported value and uncertainty as the center and width of the prior distributions, respectively. Our truncated distributions for all stars are bounded by the grid limits described in Table 2.

Finally, we include a third class of prior distributions in our model which are shared by some stars but not all. Each star within the same cluster is assumed to have the same age, metallicity, and initial Helium abundance, while these parameters should be fully independent for each target in the asteroseismic sample and for the sun. These prior distributions share the same truncated normal form as the independent parameters, but can be selectively applied to specific subsets of the data.

With our priors and likelihoods defined, we sampled the model parameters. The ANN provides derivates of the model, allowing us to utilize No-U-Turn Sampling (NUTS; Hoffman & Gelman 2014). We constructed a probabilistic model with PyMC3 (Salvatier et al. 2016), then calculated the maximum a posteriori estimate as our starting point and sampled 4 chains for 5,000 draws with 1,000 tuning steps. We sampled chains long enough to ensure that the Gelman-Rubin $\hat{R}$ statistic (Gelman & Rubin 1992) was lower than 1.01 for all parameters and that our model was well-converged.

4. RESULTS

We optimize the parameters of our model under two different assumptions—standard spindown and WMB. In the standard spindown framework, we assume stars follow a Skumanich-like angular momentum loss law, where $\dot{J} \propto \omega^3$ at late times. Under the WMB assumption, stars lose angular momentum to magnetized stellar winds with the same relation as the standard spindown law until they reach a critical Rossby number $\mathrm{Ro}_{\mathrm{crit}}$, at which point angular momentum is conserved. We use the MESA ANN as our primary emulator as its grid physics match the models used in the asteroseismic parameter estimates. In the standard spindown case, we only optimize for f_K, and retrieve a constraint of $f_K = 6.49 \pm 0.73$. For the WMB model, we report $f_K = 5.80 \pm 0.51$ and $\mathrm{Ro}_{\mathrm{crit}}/\mathrm{Ro}_{\odot} = 0.91 \pm 0.04$.

Figure 3 shows the distribution of rotation periods predicted by our WMB model. We have divided the sample into equal-size bins in $\mathrm{T}_{\mathrm{eff}}$ because temperature captures the effects of both a star's mass and metallicity on its rotational evolution. The red shaded regions show the density of stars drawn from a simulated population of 1,000,000 stars under the best-fit WMB assumptions, generated with stellar properties drawn from uniform distributions covering the parameters of our sample using our MESA emulator. The width of the distribution is caused by the range of masses, metallicities, Helium abundances, and mixing length parameters within each $\mathrm{T}_{\mathrm{eff}}$ bin. Stars in clusters can be seen as groups with discrete, well-constrained ages below 2.5 Gyr, and are valuable calibrators for the early angular momentum loss $\dot{J}$. In our model, this early $\dot{J}$ is captured by the braking law strength parameter, f_K. Stars in our asteroseismic sample span a wide range of ages, particularly on the second half of the main sequence, and provide the constraint on $\mathrm{Ro}_{\mathrm{crit}}$.

In Figure 4, we show the comparison between the rotation periods predicted by both the standard spindown and WMB models (in blue and red, respectively). Each shaded region represents the density of points in a population of 100,000 simulated stars from our MESA emulator. The standard spindown model was fit to the full sample, without allowing angular momentum conservation beyond a Rossby threshold. The models produce similar constraints on f_K, as the early rate of $\dot{J}$ is well-constrained by the clusters in both models. At older ages, the standard spindown model significantly overpredicts the rotation periods of stars in our asteroseismic sample.

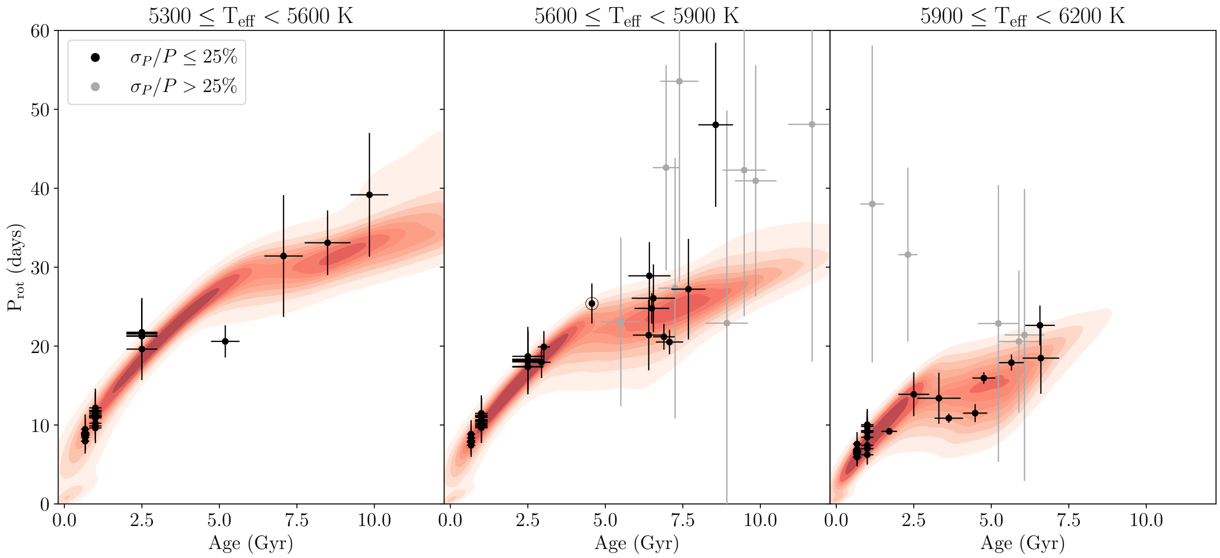

Figure 3. Stellar rotation period versus age, shown in three bins each spanning 300 K in T_{eff}. Asteroseismic measurements and cluster stars are shown by points—black points represent rotation periods with fractional uncertainties $\sigma_P/P \leq 25\%$ and gray points show $\sigma_P/P > 25\%$. The sun is marked by the $\odot$ symbol. Red contours represent the distribution of rotation periods within a given T_{eff} bin predicted by our MESA emulator model, produced from a sample of one million emulated stars with stellar properties randomly drawn from uniform distributions bounded by our sample, and f_K and Ro_{crit} fixed to the median values of the posterior distributions.

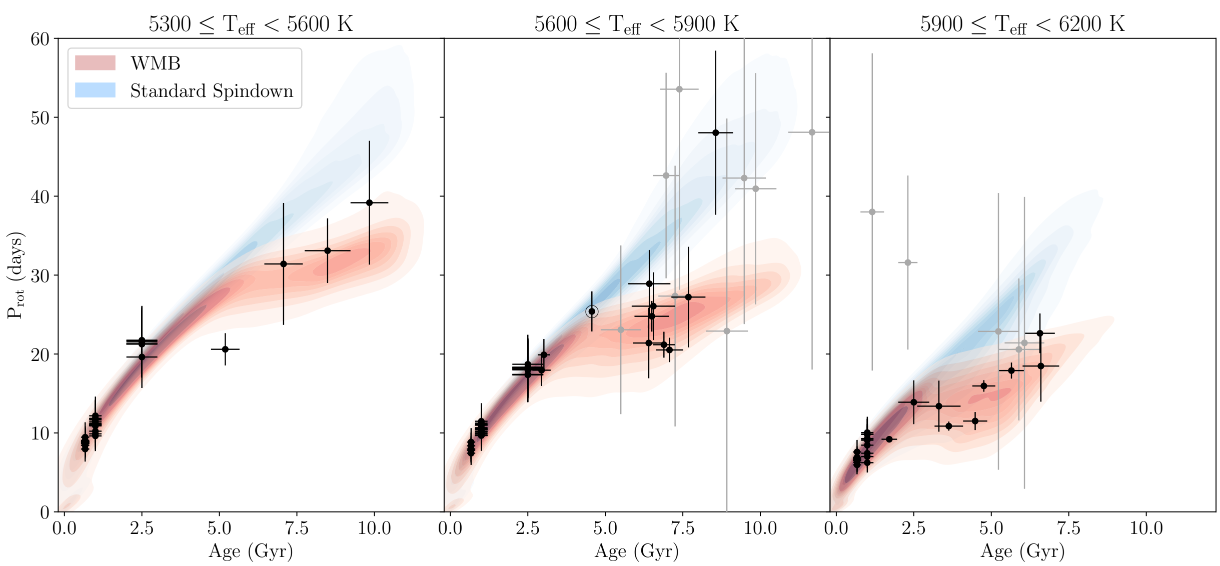

Figure 4. Same as Figure 3, with the additional comparison to the standard spindown model. The contours represent the distribution of predicted rotation periods within a given T_{eff} bin, with red showing our WMB model and blue showing a standard Skumanich-like spindown model, both generated with our MESA emulator. The value of f_K for the standard spindown model is the median value from the posterior of a fit to our full sample with no Ro_{crit} constraint.

The WMB model results in a smaller average deviation from the observed rotation periods. Figure 5 shows the the difference between predicted and observed rotation periods for our sample. The colored points show the uncertainty-weighted median within a 0.2 $t/t_{\rm MS}$ bin. On average, the standard spindown model overpredicts rotation periods by 0.72 days for the full sample and 6.00 days for stars beyond the first half of the main sequence ($t/t_{\rm MS} \geq 0.5$). Conversely, WMB underpredicts rotation periods by 0.31 days for the full sample and 3.18 days for stars past $0.5t/t_{\rm MS}$. Isolating only the asteroseismic sample (at all ages), standard spindown overpredicts $P_{\rm rot}$ by 4.66 days on average, and WMB underpredicts by 2.02 days. The corresponding fractional deviations for the asteroseismic sample are +17.73% for standard spindown and −9.09% for WMB.

Figure 5 shows the difference between predicted and observed rotation periods as a function of fraction of main sequence lifetime. For the first half of the main sequence, the standard spindown and WMB models both describe the observed rotation periods well. However, at roughly halfway though the main sequence ($0.5t/t_{\rm MS}$), the standard spindown model deviates from the observed distribution and begins overpredicting rotation periods. Both models are consistent with the cluster data, which follow a tight spindown sequence that is nearly identical for the two models (see Figure 4).

5. DISCUSSION

We have provided refined probabilistic estimates for the onset of WMB, described by the parameter $\rm Ro_{crit}$. Our model indicates that stars enter a phase of weakened braking before reaching the Rossby number of the sun ($\rm Ro_{crit} = 0.94 \pm 0.04\ Ro_{\odot}$). This result supports constraints by David et al. (2022), which found a sub-solar $\rm Ro_{crit}$ when examining the pileup in the temperature-period distribution of *Kepler* stars. van Saders et al. (2016, 2019) found that a critical Rossby number of $\rm Ro_{crit} = Ro_{\odot}$ provided the best fit to the observed rotation periods, which agrees with our results within 2σ.

The new constraints on weakened braking parameters provided here can be used as guidelines for where gyrochronology is likely to be accurate. Beyond $\rm Ro_{crit}$, stars can be observed with the same rotation period for Gyr timescales, challenging any gyrochronological estimate. We show that gyrochonological ages should be precise until $\sim\rm Ro_{\odot}$, corresponding to an age of ∼4 Gyr for sun-like stars. After the onset of WMB, age estimates should have significantly larger uncertainties due to the sustained rapid rotation on the second half of the main sequence.

5.1. *WMB Model Performance*

Towards the end of the main sequence, our model for weakened braking begins to underestimate rotation periods. This likely reflects our overly simple implementation of the transition from standard to weakened braking. The immediate shutdown of angular momentum loss beyond $\rm Ro_{crit}$ is the simplest model which introduces the fewest new parameters. Given the limited sample of reliable calibrators spanning a wide range of $\rm T_{eff}$ near the onset of WMB, any parameterization of a possible gradual transition is not well posed. As more seismic constraints are placed on the ages and rotation periods near $\rm Ro_{crit}$, additional parameters that lead to a gradual transition can be tested.

The deviation between the WMB model and observed rotation periods could additionally be explained by small deviations in inferred model ages. At the end of a star's main sequence lifetime, even in the WMB framework when angular momentum is conserved, the rotation period increases steeply due to the changing stellar moment of inertia as the star's radius expands. Models for rotation increase on short time spans in parallel tracks as stars ascend the subgiant branch, with small

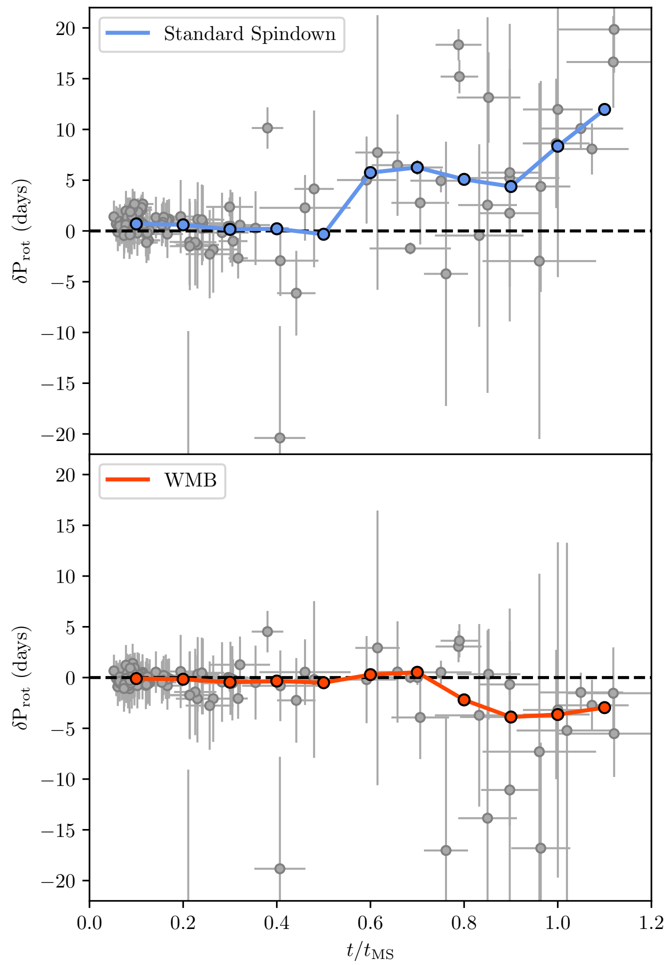

Figure 5. Difference between predicted and observed rotation periods for all stars in our sample (shown as gray points) as a function of fraction of main sequence lifetime $t/t_{\rm MS}$. The blue and red points represent the uncertainty-weighted median of δP within a 0.2 $t/t_{\rm MS}$ bin for the standard and WMB models, respectively. Main sequence lifetime was estimated by identifying the age of core-H exhaustion in MESA models generated for each star. Roughly halfway through the main sequence lifetime, the standard spindown model begins significantly over-predicting rotation periods. The WMB model is consistent with the observed distribution until near the end of the main sequence, at which point it underestimates rotation periods.

separations between stars of different $T_{\rm eff}$. Improved asteroseismic modeling, or a larger sample of stars with asteroseismic parameter constraints, could better distinguish between these effects at the end of the main sequence.

5.2. *Assessing the Asteroseismic Constraint*

To illustrate the impact of the asteroseismic sample on our ability to constrain $\mathrm{Ro_{crit}}$, we fit our model to two subsets of the data: one comprised of only clusters and the sun, capturing the early rotational evolution, and one that adds the asteroseismic stars. Figure 6 shows a Kernel Density Estimate (KDE) of the sampled marginal posterior distributions for $\mathrm{Ro_{crit}}$ when fit to each of these samples. When fit to only clusters and the sun, $\mathrm{Ro_{crit}}$ has little to no likelihood below the solar value, and is unconstrained beyond the solar value. This aligns with our expectations, as we do not expect the majority of stars in this sample to have experienced WMB. When the asteroseismic sample is included, the posterior becomes tightly constrained near the solar value. This exercise clearly demonstrates why the effects of WMB were not identified until a large enough sample of stars with precise rotation periods and ages spanning the main sequence were available.

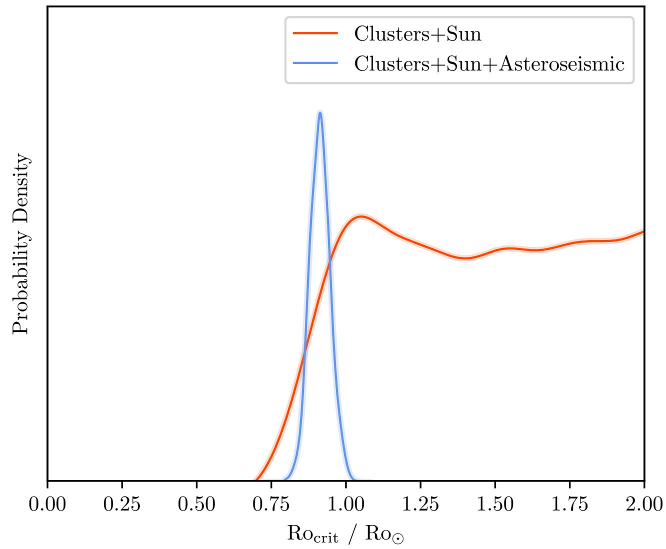

Figure 6. Comparison between posterior distributions for $\mathrm{Ro_{crit}}$ from models fit to different subsets of the data. When fit to only the clusters and sun (shown in red), $\mathrm{Ro_{crit}}$ is unconstrained beyond the solar Rossby number. With the inclusion of the asteroseismic sample (shown in blue), $\mathrm{Ro_{crit}}$ is tightly constrained just below the solar Rossby number. The y-axis has been arbitrarily scaled for clarity.

5.3. *Consistency with Solar Twins*

A recent study by Lorenzo-Oliveira et al. (2019) proposed tension between the weakened magnetic braking model and an observed population of "solar twins." The stars in this sample have typical masses within ± 0.05 $\mathrm{M_{\odot}}$ of solar and metallicities with ± 0.04 dex of solar. Rotation periods were not directly measured for the majority of stars in this sample, instead the projected rotational velocity $v \sin i$ of each star was estimated from spectral line broadening. This was converted to a projected rotation period, $P_{\mathrm{rot}}/\sin i$, using stellar properties derived from from *Gaia* DR2 (Gaia Collaboration et al. 2018) and ground-based spectroscopic data.

If a system is observed directly edge on ($i = 90°$), the projected rotation period will match that measured from photometric spot modulation or asteroseismic mode splitting. The primary effect of rotation axis inclination away from 90° is to shift the projected rotation period to a higher value (see panel (a) of Figure 7). Lorenzo-Oliveira et al. (2019) undergo a selection process of simulating projected rotation periods given some random orientation between 0 and 90°, comparing their measured population against these simulations, and reducing their sample to stars they found most likely to be seen edge on based on the agreement (see §2 of Lorenzo-Oliveira et al. 2019 for a full description of their approach). As only a fraction of the observed sample is likely to be observed directly edge on, the fastest rotation periods in the solar twins sample represent a lower envelope to the true distribution of rotation periods of the sample.

We test the standard spindown and WMB models against the solar twins sample, seen in panels (b) and (c) of Figure 7. We calculate $P_{\rm rot}/\sin i$ for our MESA emulator model tracks, drawing inclinations randomly from a uniform distribution between 0 and 1 in $\cos i$. The stellar properties of our model grid were drawn from uniform distributions bounded by the parameter cuts described in Lorenzo-Oliveira et al. (2019). We find that the standard spindown model overpredicts projected rotation periods beyond the age of the sun. The WMB model predicts the observed population with minor deviations from entirely edge-on inclinations.

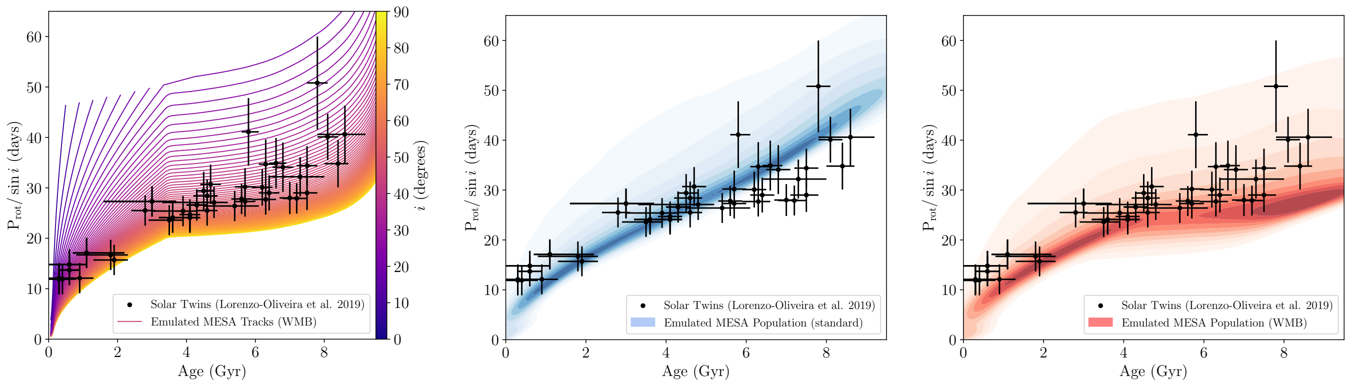

(a) (b) (c)

Figure 7. **(a)** Projected rotation period, $P_{\rm rot}/\sin i$, of the solar twins sample versus age. The colored lines show tracks from our MESA emulator for a solar-calibrated model with a range of stellar inclinations, evolved under WMB assumptions. Models that are not observed edge on have their projected periods shifted to higher values. **(b)** The solar twins sample compared to a standard spindown model with a range of stellar inclinations. We generated a population of 1,000,000 stars with parameters drawn from uniform distributions within ± 0.05 $M_\odot$ of solar for M, ± 0.04 dex of solar for [Fe/H], and inclinations, i, drawn from a uniform distribution in $\cos i$. $Y_{\rm init}$ and $\alpha_{\rm MLT}$ were drawn from uniform distributions covering our model grid. **(c)** Same as panel (b), but with the WMB model. f_K and $\mathrm{Ro_{crit}}$ were fixed to values fit to our full sample. The standard model overpredicts rotation periods of the solar twins sample beyond the age of the sun, while they are consistent with WMB when accounting for inclinations.

5.4. *Accounting for Grid Bias*

We test our model fit using neural networks trained on grids of models generated by two stellar evolution codes, MESA and YREC. This provides an opportunity to independently validate our results as well as test for any bias introduced by the choice of grid. Our MESA grid was constructed with input physics matching the asteroseismic modeling, avoiding the cross-grid bias when fitting the MESA-trained neural network to the asteroseismic observations.

The primary difference between the construction of the grids was to vary $\mathrm{Y_{init}}$ as an additional dimension of the MESA grid, while calculating it with a fixed He-enrichment law in the YREC grid. We used a relation to compute the value of $\mathrm{Y_{init}}$ for a model in the YREC grid given its metallicity [Fe/H] given by

$$Y_{\rm init} = Y_P + \frac{(1 - Y_P)\left(\frac{\mathrm{d}Y}{\mathrm{d}Z}\right)_\odot}{\left(\frac{\mathrm{d}Y}{\mathrm{d}Z}\right)_\odot + \left(\frac{Z}{X}\right)_\odot^{-[\mathrm{Fe/H}]} + 1}$$

where Y_P is the primordial Helium abundance, the slope of the Helium enrichment law that matches the solar value is $\left(\frac{dY}{dZ}\right)_\odot = 1.296$, and the solar metal fraction is $\left(\frac{Z}{X}\right)_\odot = 0.02289$ (Grevesse & Sauval 1998).

The ANN for the YREC grid was trained identically to the process for the MESA grid described in §3.4, and we constructed the probabilistic model following the process described in §3.5. For the YREC ANN, the value of $Y_{\rm init}$ fit by our asteroseismic modeling with ASTEC was not used as a constraint on the model likelihood, while it was for the MESA ANN. The choice to include $Y_{\rm init}$ as a free parameter, as well as the differences between how different stellar evolution codes calculate quantities used in our modeling, have the potential to introduce systematic biases in the resulting model fits. Here, we compare between the results inferred by emulators trained on different model grids.

Most braking laws include a strong Ro dependence, and thus a dependence on the convective overturn timescale $\tau_{\rm CZ}$, and there is no single agreed upon means of calculating this value (see Kim & Demarque 1996). Furthermore, changes in grid physics can result in different values of $\tau_{\rm CZ}$, even in solar-calibrated models. To account for this, we normalize $\rm Ro_{crit}$ by a grid-dependent solar Rossby number $\rm Ro_\odot$. To calculate $\rm Ro_\odot$ for each grid, we produced solar-calibrated stellar evolution tracks and compute the Rossby number at the age of the sun. For each model grid, we also compute the value of f_K that reproduced solar rotation at solar age under the standard spindown assumption, and apply this as a normalization factor when comparing the inferred values of f_K in our WMB models. We notate this solar-normalized braking law strength as f'_K. These normalization factors allow us to compare directly between the braking law parameters inferred from the ANN trained on each model grid.

The left panel of Figure 8 shows the marginal and joint posterior distributions for the braking law parameters when fit with the MESA and YREC ANNs. The black dashed line shows the solar Rossby number, $\rm Ro_\odot$. Both MESA and YREC return values of $\rm Ro_{crit}$ below $\rm Ro_\odot$, indicating that the onset of WMB occurs before the age of the sun for a solar analog. The inferred braking law parameters have slight offsets, but agree within 1σ. To assess the impact of leaving the $Y_{\rm init}$ parameter free, we also performed probabilistic modeling with the MESA ANN with $Y_{\rm init}$ set to the He-enrichment law described above. We show the updated posterior distributions for this fit compared to the YREC ANN in the right panel of Figure 8.

Using the YREC emulator model, we retrieve constraints on the braking law parameters of $f'_K = 0.76 \pm 0.06$ and $\rm Ro_{crit} = 0.91 \pm 0.04$. When $Y_{\rm init}$ is left as a free parameter, the MESA emulator model returns $f'_K = 0.76 \pm 0.06$ and $\rm Ro_{crit} = 0.91 \pm 0.04$. When we fix the Helium enrichment law to that used in the YREC grid, the MESA emulator model reports $f'_K = 0.78 \pm 0.07$ and $\rm Ro_{crit} = 0.94 \pm 0.04$. We note that all models consistently return a value of $\rm Ro_{crit}$ below the solar Rossby number.

When holding $Y_{\rm init}$ fixed to the YREC He-enrichment law, we find closer agreement between the braking law parameters inferred by our model fitting, with $\rm Ro_{crit}$ in near-perfect agreement. This implies that $Y_{\rm init}$ provides additional constraints on the braking law parameters, and its inclusion as a grid dimension can influence the result. $Y_{\rm init}$ is a challenging property to measure for sun-like stars, and yet affects our inferred value of $\rm Ro_{crit}$ at the $\sim 1\sigma$-level. We conclude that uncertainty in the Helium enrichment law should be treated as a systematic uncertainty in the inference of $\rm Ro_{crit}$.

5.5. *Future Applications*

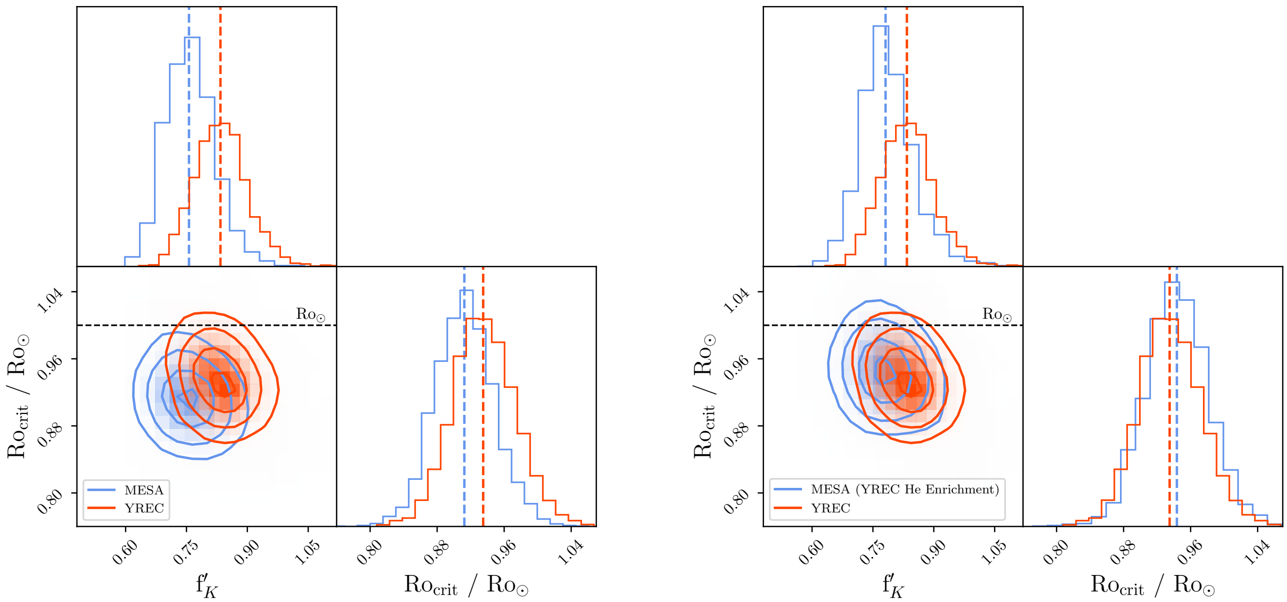

(a) (b)

Figure 8. **(a)** Corner plot showing the marginal and joint posterior distributions for the global parameters of our WMB model. Blue shows the samples from the fit using a neural net trained on a grid of MESA models, and red shows the samples from a fit using the YREC-trained neural net. The solar Rossby number $\mathrm{Ro}_\odot$ is shown as a dashed black line. The median values of each distribution are shown as dashed lines in their respective colors in the top and right panels. **(b)** The same posterior distributions, now with the He-enrichment law in the MESA probabilistic model fixed to the relation used when generating the YREC grid. The primary difference between the grids used to train the emulator models is the varied Helium abundance Y_{init} in the MESA grid. When fixed to the YREC enrichment law, the constraints on WMB global parameters are in closer agreement.

In this study, we focus only on f_K and $\mathrm{Ro}_{\mathrm{crit}}$ due to the age distribution of our sample. In the future, the same approach described here could be applied to a sample of targets which span earlier phases of evolution (i.e. young open clusters), at which time the dominant parameters in the rotation distribution will include disk-locking timescale and disk lifetime.

We limited the range of our input model grid to cover the parameters of our sample in order to reduce the computational time required for model generation and neural network training. The framework for the ANN emulator could easily be applied to a grid spanning a wider range of stellar properties, and would provide a useful tool for quickly evaluating stellar evolution tracks or simulating stellar populations. To reduce training time, the grid resolution could be selectively increased to reach a precision threshold. Scutt et al. (2023) showed that parameter spacing can be modified in different regions of the grid to improve ANN precision.

Asteroseismic pulsation frequencies are often generated alongside stellar models using tools such as GYRE (Townsend & Teitler 2013). These pulsation frequencies can be included in the grid dimensions (e.g. Lyttle et al. 2021) and applied as further likelihood constraints for models. Ideally, some combination of the above additions could be implemented to produce a broadly applicable stellar evolution emulator that does not require generating or interpolating large model grids.

6. CONCLUSIONS

In summary, our primary conclusions are:

1. We present evidence for weakened magnetic braking in old stars. Using a neural network as a stellar evolution emulator, we perform probabilistic modeling to produce posterior distributions for the parameters of the weakened braking model. We find that the weakened braking model provides the best fit to the observed distribution of rotation periods.

2. We show that the most likely weakened braking scenario diverges from standard spindown at a slightly earlier evolutionary phase than the sun. We caution that our WMB model is a simplified case in which angular momentum loss is fully switched off at a critical Rossby number, and likely does not fully capture the time evolution of the stellar dynamo; therefore, it remains challenging to infer the precise onset of WMB relative to the sun's evolution.

3. Our method for emulating stellar evolution with a neural network enables rapid evaluation of stellar models, making it possible to test a wide range of prescriptions for magnetic braking. By modifying the braking law used to generate our training set, we could test other effects at early times, such as the impact of core-envelope decoupling or disk-locking.

4. We report mild disagreement between the constraints on WMB parameters when using different underlying model grids. This indicates that the choice of grid physics and which parameters are varied in the model can impact the inferred model parameters.

5. The growing population of stars with precisely measured ages and rotation periods from asteroseismology is shedding essential light on the evolution of stellar rotation. As additional stars are added to this sample, the transition to WMB can be constrained to higher precision.

6. Our constraint on the $\mathrm{Ro_{crit}}$ at which stars enter a phase of weakened braking suggests that gyrochronology faces challenges when estimating stellar ages for much of the main sequence lifetime. For sun-like stars, gyrochronological age estimates are likely unreliable beyond an age of $\sim$4 Gyr. For more massive stars ($\gtrsim 1.1\mathrm{M_\odot}$), gyrochronology relations appear break down even earlier, at an age of $\sim$2.5 Gyr.

7. Even after a star has entered the weakened braking phase, a reasonable range for its age can be estimated from its rotation period, and our constraint on $\mathrm{Ro_{crit}}$ enables gyrochronological modeling that will provide a realistic uncertainty on the stellar age.

ACKNOWLEDGEMENTS

N.S. acknowledges support by the National Science Foundation Graduate Research Fellowship Program under Grant No. 1842402.

REFERENCES

Abadi, M., Barham, P., Chen, J., et al. 2016, TensorFlow: A System for Large-Scale Machine Learning, arXiv. http://ascl.net/1605.08695

Adelberger, E. G., Balantekin, A. B., Bemmerer, D., et al. 2011, Reviews of Modern Physics, 83, 195, doi: 10.1103/RevModPhys.83.195

Angus, R., Aigrain, S., Foreman-Mackey, D., & McQuillan, A. 2015, Monthly Notices of the Royal Astronomical Society, 450, 1787, doi: 10.1093/mnras/stv423

Angus, R., Morton, T. D., Foreman-Mackey, D., et al. 2019, The Astronomical Journal, 158, 173, doi: 10.3847/1538-3881/ab3c53

Ball, W. H., & Gizon, L. 2014, A&A, 568, A123, doi: 10.1051/0004-6361/201424325

Barnes, S. A. 2007, The Astrophysical Journal, 669, 1167, doi: 10.1086/519295

—. 2010, The Astrophysical Journal, 722, 222, doi: 10.1088/0004-637X/722/1/222

Berger, T. A., Huber, D., van Saders, J. L., et al. 2020, The Astronomical Journal, 159, 280, doi: 10.3847/1538-3881/159/6/280

Borucki, W. J., Koch, D., Basri, G., et al. 2010, Science, 327, 977, doi: 10.1126/science.1185402

Chaplin, W. J., Bedding, T. R., Bonanno, A., et al. 2011, The Astrophysical Journal, 732, L5, doi: 10.1088/2041-8205/732/1/L5

Cody, A. M., Barentsen, G., Hedges, C., et al. 2018, Research Notes of the AAS, 2, 199, doi: 10.3847/2515-5172/aaec76

Cox, J. P., & Giuli, R. T. 1968, Principles of stellar structure

Creevey, O., Metcalfe, T. S., Schultheis, M., et al. 2017, Astronomy & Astrophysics, 601, A67, doi: 10.1051/0004-6361/201629496

Curtis, J. L., Agüeros, M. A., Douglas, S. T., & Meibom, S. 2019, The Astrophysical Journal, 879, 49, doi: 10.3847/1538-4357/ab2393

Curtis, J. L., Agüeros, M. A., Matt, S. P., et al. 2020, The Astrophysical Journal, 904, 140, doi: 10.3847/1538-4357/abbf58

David, T. J., Angus, R., Curtis, J. L., et al. 2022, The Astrophysical Journal, 933, 114, doi: 10.3847/1538-4357/ac6dd3

Davies, G. R., Chaplin, W. J., Farr, W. M., et al. 2015, Monthly Notices of the Royal Astronomical Society, 446, 2959, doi: 10.1093/mnras/stu2331

Demarque, P., Guenther, D. B., Li, L. H., Mazumdar, A., & Straka, C. W. 2008, Astrophysics and Space Science, 316, 31, doi: 10.1007/s10509-007-9698-y

Denissenkov, P. A., Pinsonneault, M., Terndrup, D. M., & Newsham, G. 2010, The Astrophysical Journal, 716, 1269, doi: 10.1088/0004-637X/716/2/1269

dos Santos, L. A., Meléndez, J., do Nascimento, J.-D., et al. 2016, Astronomy & Astrophysics, 592, A156, doi: 10.1051/0004-6361/201628558

Dungee, R., van Saders, J., Gaidos, E., et al. 2022, The Astrophysical Journal, 938, 118, doi: 10.3847/1538-4357/ac90be

Epstein, C. R., & Pinsonneault, M. H. 2013, The Astrophysical Journal, 780, 159, doi: 10.1088/0004-637X/780/2/159

Gaia Collaboration, Brown, A. G. A., Vallenari, A., et al. 2018, Astronomy & Astrophysics, 616, A1, doi: 10.1051/0004-6361/201833051

Gallet, F., & Bouvier, J. 2013, Astronomy & Astrophysics, 556, A36, doi: 10.1051/0004-6361/201321302

—. 2015, Astronomy & Astrophysics, 577, A98, doi: 10.1051/0004-6361/201525660

Garraffo, C., Drake, J. J., & Cohen, O. 2016, Astronomy & Astrophysics, 595, A110, doi: 10.1051/0004-6361/201628367

Gelman, A., & Rubin, D. B. 1992, Statistical Science, 7, 457, doi: 10.1214/ss/1177011136

Grevesse, N., & Sauval, A. 1998, Space Science Reviews, 85, 161, doi: 10.1023/A:1005161325181

Hall, O. J., Davies, G. R., van Saders, J., et al. 2021, Nature Astronomy, doi: 10.1038/s41550-021-01335-x

Howell, S., Sobeck, C., Haas, M. R., et al. 2014, Publications of the Astronomical Society of the Pacific, 126, 398, doi: 10.1086/676406

Hoffman, M. D., & Gelman, A. 2014, Journal of Machine Learning Research, 15, 1351

Huber, D., Bedding, T. R., Stello, D., et al. 2011, The Astrophysical Journal, 743, 143, doi: 10.1088/0004-637X/743/2/143

Kawaler, S. D. 1988, The Astrophysical Journal, 333, 236, doi: 10.1086/166740

Kim, Y.-C., & Demarque, P. 1996, ApJ, 457, 340, doi: 10.1086/176733

Kingma, D. P., & Ba, J. 2017, Adam: A Method for Stochastic Optimization, arXiv. http://ascl.net/1412.6980

Krishnamurthi, A., Pinsonneault, M. H., Barnes, S., & Sofia, S. 1997, The Astrophysical Journal, 480, 303, doi: 10.1086/303958

Kurucz, R. L. 1997, in The Third Conference on Faint Blue Stars, ed. A. G. D. Philip, J. Liebert, R. Saffer, & D. S. Hayes, 33

Lorenzo-Oliveira, D., Meléndez, J., Galarza, J. Y., et al. 2019, Monthly Notices of the Royal Astronomical Society: Letters, 485, L68, doi: 10.1093/mnrasl/slz034

Lyttle, A. J., Davies, G. R., Li, T., et al. 2021, arXiv:2105.04482 [astro-ph]. https://arxiv.org/abs/2105.04482

Mamajek, E. E., & Hillenbrand, L. A. 2008, The Astrophysical Journal, 687, 1264, doi: 10.1086/591785

Matt, S. P., Brun, A. S., Baraffe, I., Bouvier, J., & Chabrier, G. 2015, The Astrophysical Journal Letters, 799, L23, doi: 10.1088/2041-8205/799/2/L23

Matt, S. P., MacGregor, K. B., Pinsonneault, M. H., & Greene, T. P. 2012, The Astrophysical Journal, 754, L26, doi: 10.1088/2041-8205/754/2/L26

McQuillan, A., Mazeh, T., & Aigrain, S. 2014, The Astrophysical Journal Supplement Series, 211, 24, doi: 10.1088/0067-0049/211/2/24

Meibom, S., Barnes, S. A., Platais, I., et al. 2015, Nature, 517, 589, doi: 10.1038/nature14118

Meibom, S., Barnes, S. A., Latham, D. W., et al. 2011, The Astrophysical Journal, 733, L9, doi: 10.1088/2041-8205/733/1/L9

Mendoza, C., Seaton, M. J., Buerger, P., et al. 2007, Monthly Notices of the Royal Astronomical Society, 378, 1031, doi: 10.1111/j.1365-2966.2007.11837.x

Metcalfe, T. S., & Charbonneau, P. 2003, Journal of Computational Physics, 185, 176, doi: 10.1016/S0021-9991(02)00053-0

Metcalfe, T. S., Creevey, O. L., & Christensen-Dalsgaard, J. 2009, ApJ, 699, 373, doi: 10.1088/0004-637X/699/1/373

Metcalfe, T. S., Egeland, R., & van Saders, J. 2016, The Astrophysical Journal, 826, L2, doi: 10.3847/2041-8205/826/1/L2

Metcalfe, T. S., Kochukhov, O., Ilyin, I. V., et al. 2019, The Astrophysical Journal Letters, 887, L38, doi: 10.3847/2041-8213/ab5e48

Metcalfe, T. S., Creevey, O. L., Dogan, G., et al. 2014, The Astrophysical Journal Supplement Series, 214, 27, doi: 10.1088/0067-0049/214/2/27

Metcalfe, T. S., van Saders, J. L., Basu, S., et al. 2020, The Astrophysical Journal, 900, 154, doi: 10.3847/1538-4357/aba963

Nielsen, M. B., Schunker, H., Gizon, L., & Ball, W. H. 2015, Astronomy & Astrophysics, 582, A10, doi: 10.1051/0004-6361/201526615

Parker, E. N. 1958, The Astrophysical Journal, 128, 664, doi: 10.1086/146579

Paxton, B., Bildsten, L., Dotter, A., et al. 2010, The Astrophysical Journal Supplement Series, 192, 3, doi: 10.1088/0067-0049/192/1/3

Paxton, B., Cantiello, M., Arras, P., et al. 2013, The Astrophysical Journal Supplement Series, 208, 4, doi: 10.1088/0067-0049/208/1/4

Paxton, B., Marchant, P., Schwab, J., et al. 2015, The Astrophysical Journal Supplement Series, 220, 15, doi: 10.1088/0067-0049/220/1/15

Paxton, B., Schwab, J., Bauer, E. B., et al. 2018, The Astrophysical Journal Supplement Series, 234, 34, doi: 10.3847/1538-4365/aaa5a8

Paxton, B., Smolec, R., Schwab, J., et al. 2019, The Astrophysical Journal Supplement Series, 243, 10, doi: 10.3847/1538-4365/ab2241

Pinsonneault, M. H., Kawaler, S. D., Sofia, S., & Demarque, P. 1989, ApJ, 338, 424, doi: 10.1086/167210

Rebull, L. M., Stauffer, J. R., Hillenbrand, L. A., et al. 2017, The Astrophysical Journal, 839, 92, doi: 10.3847/1538-4357/aa6aa4

Reiners, A., & Mohanty, S. 2012, The Astrophysical Journal, 746, 43, doi: 10.1088/0004-637X/746/1/43

Reinhold, T., Shapiro, A. I., Solanki, S. K., et al. 2020, Science, 368, 518, doi: 10.1126/science.aay3821

Réville, V., Brun, A. S., Matt, S. P., Strugarek, A., & Pinto, R. F. 2015, The Astrophysical Journal, 798, 116, doi: 10.1088/0004-637X/798/2/116

Rogers, F. J., & Nayfonov, A. 2002, ApJ, 576, 1064, doi: 10.1086/341894

Rogers, F. J., Swenson, F. J., & Iglesias, C. A. 1996, ApJ, 456, 902, doi: 10.1086/176705

Salvatier, J., Wiecki, T. V., & Fonnesbeck, C. 2016, PeerJ Computer Science, 2, e55, doi: 10.7717/peerj-cs.55

Santos, A. R. G., Breton, S. N., Mathur, S., & García, R. A. 2021, The Astrophysical Journal Supplement Series, 255, 17, doi: 10.3847/1538-4365/ac033f

Scutt, O. J., Murphy, S. J., Nielsen, M. B., et al. 2023, Asteroseismology of δ Scuti Stars: Emulating Model Grids Using a Neural Network, arXiv. http://ascl.net/2302.11025

Sills, A., Pinsonneault, M. H., & Terndrup, D. M. 2000, The Astrophysical Journal, 534, 335, doi: 10.1086/308739

Silva Aguirre, V., Davies, G. R., Basu, S., et al. 2015, Monthly Notices of the Royal Astronomical Society, 452, 2127, doi: 10.1093/mnras/stv1388

Skumanich, A. 1972, The Astrophysical Journal, 565

Spada, F., & Lanzafame, A. C. 2020, Astronomy & Astrophysics, 636, A76, doi: 10.1051/0004-6361/201936384

Tayar, J., Claytor, Z. R., Huber, D., & van Saders, J. 2020, arXiv:2012.07957 [astro-ph]. https://arxiv.org/abs/2012.07957

Thoul, A. A., Bahcall, J. N., & Loeb, A. 1994, ApJ, 421, 828, doi: 10.1086/173695

Townsend, R. H. D., & Teitler, S. A. 2013, Monthly Notices of the Royal Astronomical Society, 435, 3406, doi: 10.1093/mnras/stt1533

van Saders, J., Ceillier, T., Metcalfe, T. S., et al. 2016, Nature, 529, 181, doi: 10.1038/nature16168

van Saders, J., & Pinsonneault, M. H. 2013, The Astrophysical Journal, 776, 67, doi: 10.1088/0004-637X/776/2/67

van Saders, J., Pinsonneault, M. H., & Barbieri, M. 2019, The Astrophysical Journal, 872, 128, doi: 10.3847/1538-4357/aafafe

Vitense, E. 1953, ZA, 32, 135

Weber, E. J., & Davis, L. 1967, The Astrophysical Journal, 148

White, T. R., Benomar, O., Silva Aguirre, V., et al. 2017, Astronomy & Astrophysics, 601, A82, doi: 10.1051/0004-6361/201628706

Woitaszek, M., Metcalfe, T., & Shorrock, I. 2009, Proceedings of the 5th Grid Computing Environments Workshop on - GCE '09, 1, doi: 10.1145/1658260.1658262

APPENDIX

A. NEURAL NETWORK STRUCTURE

As described in §3.4, our artificial neural network was generated with six hidden layers of 128 neurons. A model summary can be found in Table 3.

Layer (type)	Output Shape	N_{params}
normalization (Normalization)	(None, 7)	15
dense (Dense)	(None, 128)	1024
dense_1 (Dense)	(None, 128)	16512
dense_2 (Dense)	(None, 128)	16512
dense_3 (Dense)	(None, 128)	16512
dense_4 (Dense)	(None, 128)	16512
dense_5 (Dense)	(None, 128)	16512
dense_6 (Dense)	(None, 4)	516
rescaling (Rescaling)	(None, 4)	0
Total params: 84,115		
Trainable params: 84,100		
Non-trainable params: 15		

Table 3. Model summary for our ANN.

B. MODEL VALIDATION

To validate the performance of our model, we calculated the difference between the observed value and the median of the posterior sampled distribution for each parameter in our grid. Figure 9 shows this value, where $\delta X = X_{\mathrm{predicted}} - X_{\mathrm{observed}}$ for a parameter X. We find good overall agreement between predicted and observed values, with no significant systematic offsets.

For each star in our sample, we retrieve full posterior distributions for each parameter. In Figure 10, we show the sampled marginal and joint posterior distributions for the sun.

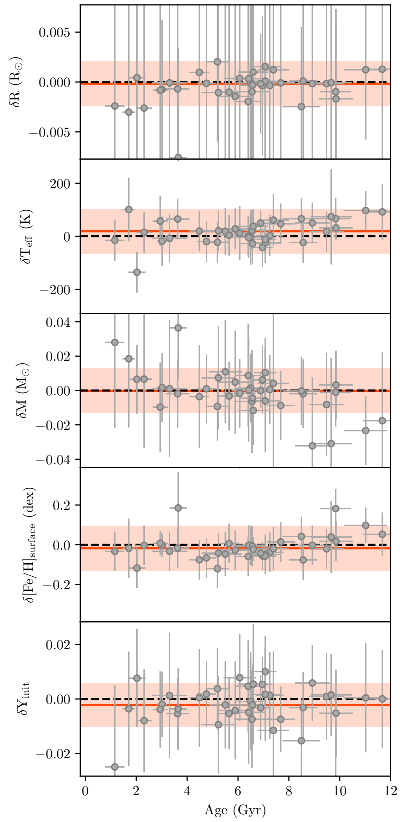

Figure 9. Difference between observed values of stellar properties and predictions from our probabilistic model (predicted−observed), plotted against stellar age. The red line shows the median of the difference, with the standard deviation shown by the shaded region.

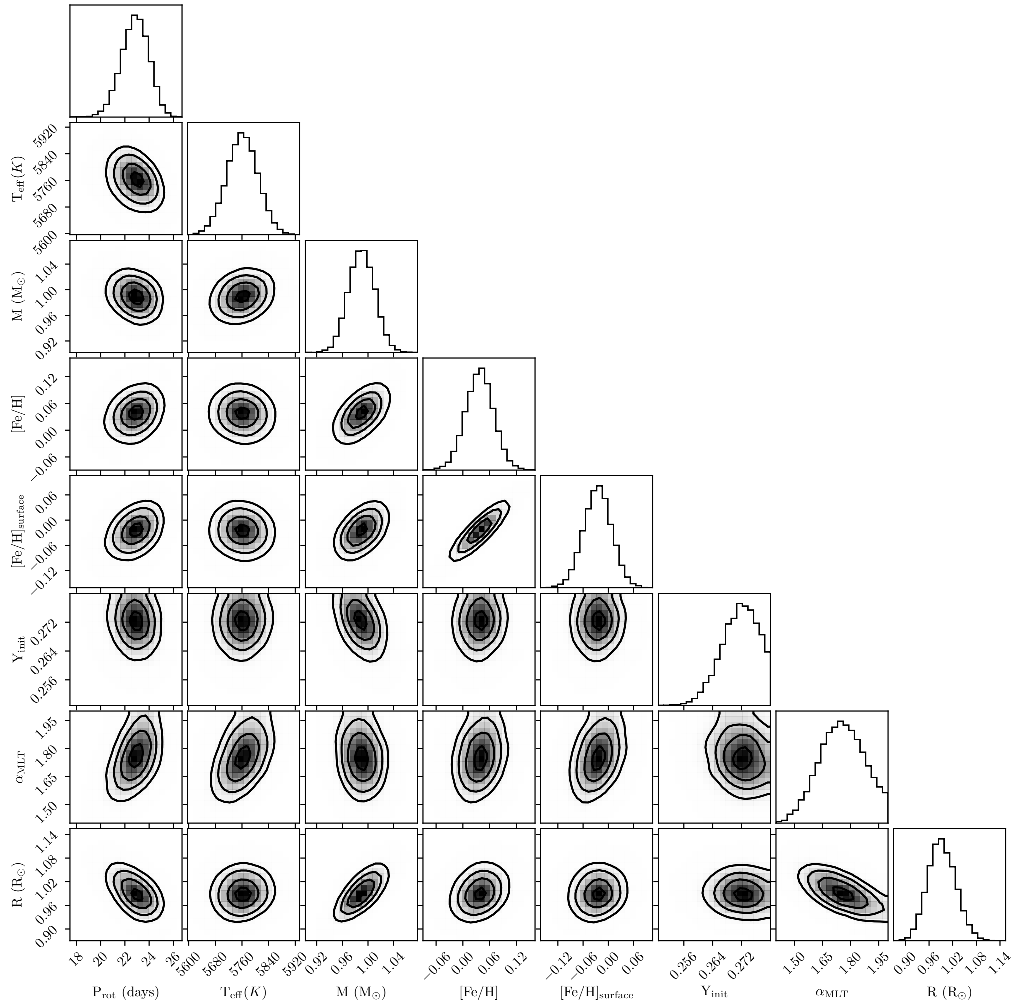

Figure 10. Corner plot showing marginal and joint posterior distributions for the sun from our sampled probabilistic model.